RSC Advances

PAPER

View Article Online
View Journal | View Issue



Cite this: *RSC Adv.*, 2022, **12**, 7935

# Catalytic graphitization assisted synthesis of $Fe_3C$/Fe/graphitic carbon with advanced pseudocapacitance†

Aoping Guo, Xiaobao Zhang, Baiyi Shao, Song Sang and Xiaojing Yang *

Received 4th December 2021
Accepted 16th February 2022

DOI: 10.1039/d1ra08834c

rsc.li/rsc-advances

We report an environmentally friendly strategy for the synthesis of $Fe_3C$/Fe/graphitic carbon based on hydrothermal carbonization and graphitization of carbon spheres with potassium ferrate ($K_2FeO_4$) at 800 °C. The obtained sample consisting of $Fe_3C$/Fe nanoparticles and graphitic carbon (FC-1-8) delivered an enhanced pseudocapacitance of 428.0 F $g^{-1}$ at a current density of 1 A $g^{-1}$. After removal of the $Fe_3C$/Fe electroactive materials, the graphitic carbon (FC-1-8-HCl) possessed a large specific surface area (SSA) up to 2813.6 $m^2$ $g^{-1}$ with a capacity of 243.3 F $g^{-1}$ at 1 A $g^{-1}$, far outweighing the other amorphous carbon electrodes of FC-0-8 (carbon spheres annealed at 800 °C without the treatment of $K_2FeO_4$). The graphitic material with a porous structure could offer more electroactive sites and improved conductivity of the sample. This method provided guidelines for the synthesis of superior performance supercapacitors with synchronous graphitic carbon and electroactive species.

## 1. Introduction

The ever-increasing demand for energy all over the world has promoted intensive research in the field of energy storage materials. Among various types of emerging power devices, supercapacitors (SCs) owing to their excellent output capability, quick charge–discharge rate and long cycle stability have attracted much attention of researchers.[1,2]

Carbon-based materials, such as activated carbon and graphene, have been regarded as the most common electrode materials. The hydrothermal carbonization technique is a green and soft chemistry method to synthesize carbon-based materials under mild temperature and self-generated pressure.[3] The whole process involved a series of reactions, such as hydrolysis, dehydration, polymerization and aromatization, leading to the formation of brown hydrochar and soluble chemicals.[4] Biomass-derived carbon materials are low-cost and have been reported as good candidates for carbon-based electrodes.[5]

The properties of specific surface area (SSA), porosity and conductivity of these materials have a big influence on their performance of electrochemistry.[6–8] As we all know, the larger SSA value is favorable to obtaining electrode material with excellent performance. Till now, various strategies have been proposed to develop porous structure, including carbonization under KOH,[9] $ZnCl_2$ (ref. 10 and 11) and $CO_2$.[12] Despite the remarkable increase in the SSA value and pore size after activation, most materials display unsatisfied specific capacitance because of the low conductivity. Creating graphitic carbon leading to lower internal resistance is a possible method to solve the problem. Generally, the conventional graphitization transformation requires rigorous conditions, like high temperature (>1000 °C) or high vacuum degree, which do not only needs a huge energy input but also leads to a decreased porosity of the host.[13,14] However, using transition metal (Fe, Co or Ni) functioned as a catalyst during the pyrolysis process could achieve graphitization transformation at low temperature.[15–17] Metal organic frameworks (MOF), as a kind of porous coordination polymers, are promising materials in the field of supercapacitor and battery.[18] Pang *et al.* studied a series of MOF composite as excellent electrochemical energy storage material, such as [Ni(thiophene-2,5-dicarboxylate)(4,4′-bipyridine)]*n* MOF nanocrystals,[19] $Co_3O_4$ nanocube@Co-MOF.[20] In some cases, the derived species could serve as electroactive species as well and can be used to prepare SCs with high performance. For example, Li *et al.*[21] fabricated carbon hybrids by g-$C_3N_4$ and iron oxalate as electrode, which delivered an enhanced pseudocapacitance. In this process, iron oxalate was further reduced to metallic Fe followed by carbide reaction. Fe-based nanomaterials, such as encapsulated FeP nanoparticles with graphene,[22] nano $Fe_7C_3$ with *in situ* grown CNT on N doped hollow carbon cube,[23] N-doped carbon nanotubes grafted onto MOF-derived carbon nanomaterials (Fe-NCNT) were proved to display efficient electrochemical performance. β-FeOOH@carbon derived multi-shelled $Fe_2O_3$ microspheres by calcination in air could deliver a high capacity up to 630 F $g^{-1}$ at 1 A $g^{-1}$.[24]

Herein, we achieved a safe and environmentally friendly transformation from amorphous carbon spheres to graphitic

*Beijing Key Laboratory of Energy Conversion and Storage Materials, College of Chemistry, Beijing Normal University, No. 19, Xinjiekouwai Street, Haidian District, Beijing 100875, China. E-mail: yang.xiaojing@bnu.edu.cn*

† Electronic supplementary information (ESI) available. See DOI: 10.1039/d1ra08834c

carbon layers with $Fe_3C$/Fe nanoparticles (NPs) through $K_2FeO_4$ named as FC-1-8, which showed excellent pseudocapacitance as the electrode for SCs. $K_2FeO_4$, in this article, is not only used as the activating agent but also functioned as the precursor of catalyst (Fe) in the graphitic transformation process. The derived $Fe_3C$/Fe NPs serve as electroactive species as well and compared with the other amorphous carbon electrodes of FC-0-8 (carbon spheres annealed without the treatment of $K_2FeO_4$), the $K_2FeO_4$-derived $Fe_3C$/Fe/graphitic carbon exhibited an outstanding pseudocapacitance of 428.0 F $g^{-1}$ at 1 A $g^{-1}$ working as an electrode material for SCs. After removal of the $Fe_3C$/Fe electroactive materials, the graphitic carbon (FC-1-8-HCl) with a much high SSA up to 2813.6 $m^2$ $g^{-1}$ displayed a capacity of two times higher than that of the other type of amorphous carbon electrode, FC-0-8. $Fe_3C$/Fe/graphitic carbon exhibited synchronous performance of graphitic carbon and electroactive species, which was inspirational and provided a novel route to design electrode material.

## 2. Experimental

### 2.1 Materials

Glucose ($C_6H_{12}O_6$, AR) was purchased from Aladdin Reagent Inc. Potassium ferrate ($K_2FeO_4$, >98%) was obtained from Beijing Innochem Chemical Co., Ltd. All the chemicals were used as received without further purification.

### 2.2 Hydrothermal synthesis of carbon spheres

The carbon spheres were synthesized using glucose as a precursor through hydrothermal carbonization. In a typical procedure, a certain concentration of glucose was transferred to a Teflon-lined stainless-steel autoclave (100 mL), followed by heating at 140–200 °C for 10 h before being naturally cooled to room temperature. The precipitates were isolated by centrifugation and rinsed sequentially with deionized water and ethanol, and dried in an oven at 60 °C overnight. Several kinds of parameters were investigated and the details were displayed in Table 1. The samples were named as $G_X$-$T$-$t$, where $X$ is the concentration of glucose, $T$ is the hydrothermal temperature, $t$ is the reaction time. For example, $G_1$-200-10 means 1 M glucose was hydrothermally treated at 200 °C for 10 h.

### 2.3 Carbonization and activation of carbon spheres

0.5 g carbon spheres were mixed with $K_2FeO_4$ powder in the mass ratio of 1 : 0 and 1 : 1 in deionized water (80 mL) stirring for 8 h. The mixture was dried in an oven overnight at 100 °C followed by annealed in Ar atmosphere under 800 °C at a heating rate of 5 °C $min^{-1}$ for 2 h. The as-obtained samples were diluted with deionized water until pH reached 7 and dried at 80 °C. The samples were denoted as FC-0-8 and FC-1-8. The yield of FC-1-8 was almost 52.5%. For comparison, FC-1-8-HCl was prepared by etching FC-1-8 with concentrated HCl and washed with deionized water to neutrality and dried at 80 °C.

Table 1 Samples prepared under different experimental conditions

| Sample designation | Glucose concentration (mol $L^{-1}$) | Temperature/°C | Time/h |
|---|---|---|---|
| $G_1$-200-10 | 1.0 | 200 | 10 |
| $G_1$-180-10 | 1.0 | 180 | 10 |
| $G_{0.5}$-180-10 | 0.5 | 180 | 10 |
| $G_{0.5}$-140-10 | 0.5 | 140 | 10 |
| $G_{0.5}$-140-20 | 0.5 | 140 | 20 |

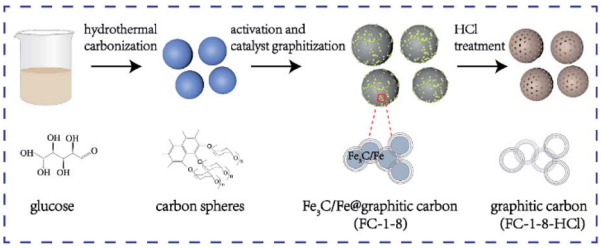


Fig. 1 Schematic illustration of synthesis procedures of the samples.

### 2.4 Characterizations

The main text of the article should appear here with headings as appropriate. A series of measurements were conducted to determine the structure of the products. The crystal structure was determined by powder X-ray diffraction (XRD) (D/MAX-1200, Rigaku Denki Co. Ltd, Japan) with a Bruker D8 Advance diffractometer equipped with Cu Kα radiation at $l = 0.15406$ nm at 40 kV and 40 mA were recorded in the range of $2\theta = 10$–70. The morphological morphology was measured using a scanning electron microscope (SEM) at 5.0 kV and a transmission

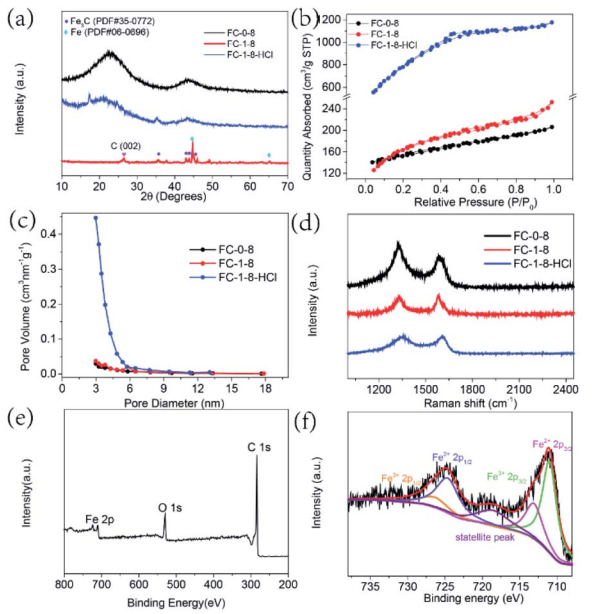


Fig. 2 (a–d) XRD, $N_2$ adsorption–desorption isotherms, pore size distribution curves and Raman spectra of FC-0-8, FC-1-8 and FC-1-8-HCl. (e and f) XPS spectra of survey and high-resolution Fe 2p of FC-1-8 sample.

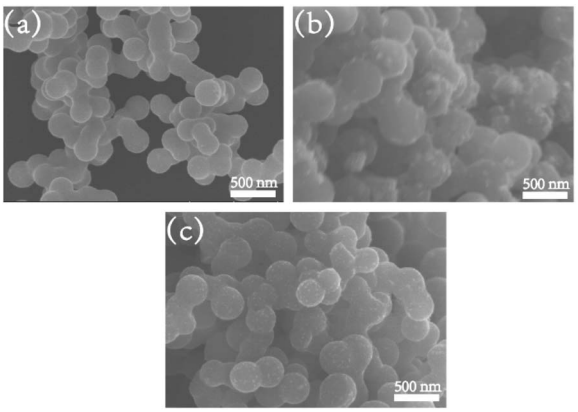


Fig. 3 SEM images with low and high resolutions of (a) FC-0-8, (b) FC-1-8 and (c) FC-1-8-HCl.

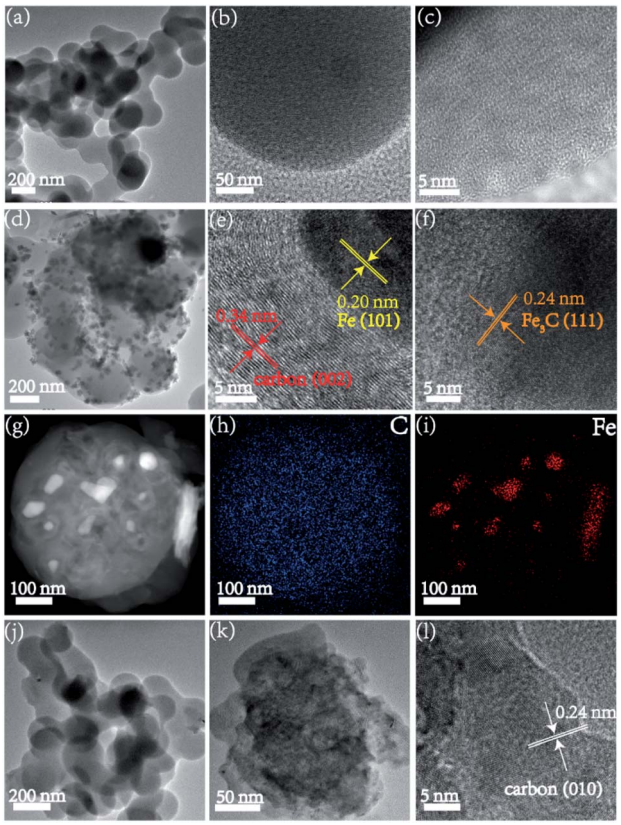


Fig. 4 TEM and HRTEM images of FC-0-8 (a–c) and FC-1-8 (d–f); (g–i) TEM image and the corresponding elemental mapping images of C and Fe in FC-1-8 sample; (j–l) TEM images and HRTEM of FC-1-8-HCl sample.

electron microscope (TEM, Talos F200S operating at 200 kV). Raman spectra were recorded from 1000 to 2500 $cm^{-1}$ on a microscopic confocal Raman spectrometer (LabRAM Aramis, Horiba Jobin Yvon) using a 532 nm YAG solid-state laser. The chemical composition of the sample was verified by X-ray photoelectron spectroscopy (XPS) analysis was conducted by 500 μm beam spot of an Escalab 250Xi electron spectrometer

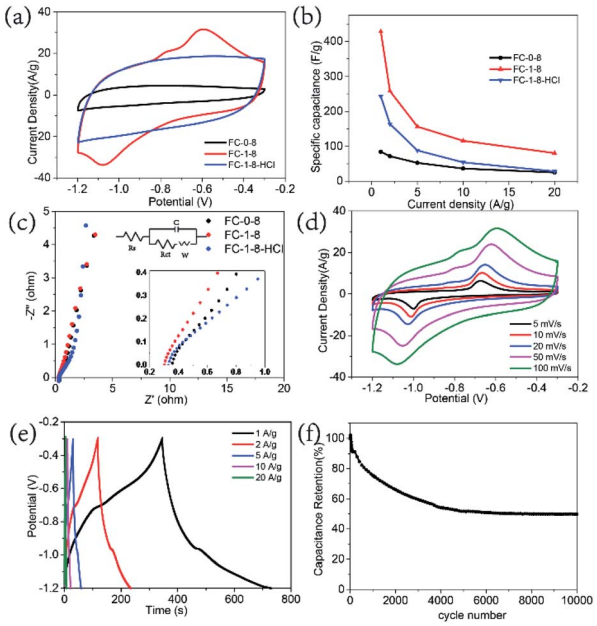


Fig. 5 (a) CV curves at a scan rate of 100 mV $s^{-1}$ of FC-0-8, FC-1-8 and FC-1-8-HCl, respectively. (b) Rate capability at a current density from 1 to 20 A $g^{-1}$ and (c) EIS of the samples. (d and e) CV curves and galvanostatic charge–discharge curves of FC-1-8. (f) Cycling performance of FC-1-8 at 5 A $g^{-1}$ for 10 000 cycles.

from Thermo Scientific Ltd, Al Kα ($h\nu = 1486.6$ eV) was used as the monoenergetic X-ray source, and the energy step size was set at 0.050 eV. The Brunauer–Emmett–Teller (BET) surface area was determined by an $N_2$ adsorption method using an automated surface area and pore-size analyzer (Autosorb-IQ2-MP-C system). The pore size distribution was calculated according to a quenched solid density functional theory (QSDFT) theory.

### 2.5 Electrochemical tests

The electrochemical properties were measured by a three-electrode system with a platinum foil as counter electrode and Hg/HgO electrode as the reference electrode. A 6 M KOH aqueous solution was used as the electrolyte. The working electrode was prepared by mixing active materials, carbon black and PTFE at a weight ratio of 8 : 1 : 1 in ethanol solvent. The slurry was mixed by ultrasonication for 2 h and then loaded on graphite paper (1 × 1 $cm^2$), followed by vacuum drying at 70 °C for 24 h.

The cyclic voltammetry (CV) and galvanostatic charge–discharge (GCD) curves were performed on an electrochemical workstation (CorrTest, China) at a voltage range from −1.2 to −0.3 V. The specific capacitance ($C$) was obtained from CV curves using the following relationship:

$$C = \frac{I \times \Delta t}{m \times \Delta V} \quad (1)$$

where $I$ is the discharge current (A), $m$ is the active material mass of the working electrode (g), $\Delta V$ is the window voltage (V), and $\Delta t$ is the discharge time (s).

Table 2 Comparison of the electrochemical performance of $Fe_3C$/Fe/graphitic carbon with reported references

| Materials | Capacitance (F $g^{-1}$) | Ref. |
|---|---|---|
| Encapsulated Fe/$Fe_3C$@C | 177 (0.1 A $g^{-1}$) | 36 |
| Fe/$Fe_3C$ | 214 (1 A $g^{-1}$) | 37 |
| $Fe_3C$/$Fe_3O_4$/C nanosheets | 315 (0.5 A $g^{-1}$) | 38 |
| N-doped carbon decorated with Fe ($Fe_3O_4$, $Fe_3C$) | 217.8 (1 A $g^{-1}$) | 39 |
| CNTs/$Fe_3C$ | 181 (0.1 A $g^{-1}$) | 40 |
| $Fe_3C$/Fe/graphitic carbon | 428.0 (1 A $g^{-1}$) | Our work |

The electrochemical impedance spectroscopy (EIS) was carried out on an electrochemical workstation (CHI660D) at an open circuit potential and a frequency range from $10^{-2}$ to $10^5$ Hz.

# 3. Results and discussion

## 3.1 Formation of carbon spheres

The brown powder synthesized through hydrothermal carbonization of glucose are spherical particles. It is worth noting that the formation of carbon spheres is influenced by hydrothermal temperature, reaction time and the concentration of glucose. SEM observations indicated that when the hydrothermal temperature decreased from 200 °C to 180 °C, the diameter of carbon spheres showed a decreased trend (Fig. S1a–d†). Moreover, the particle size distributions in Fig. S1a–d† demonstrated that the particle sizes of $G_1$-200-10 and $G_1$-180-10 were 490 nm and 235 nm accounted for a large percentage. Lower hydrothermal temperature would lead to the formation of smaller carbon spheres (Fig. S1e and f†). By adjusting the parameters of the synthesis process, we could obtain carbon spheres with the calculated average particle diameter of ~190 nm ($G_{0.5}$-180-10). However, no solid product of carbon spheres were formed except brown solutions in the case of lower hydrothermal temperature (140 °C) even with a longer reaction time of 20 h. The brown solution without the formation of carbon spheres suggested that aromatic compounds and oligosaccharides were formed in the "polymerization" step, while none of the nuclei was generated and to be continued growing.[25,26] To investigate the graphitization transformation process better, carbon spheres with a diameter of ~190 nm were chosen as the precursor.

## 3.2 Graphitization process

The fabrication procedures of graphitic samples of FC-1-8 and FC-1-8-HCl through $K_2FeO_4$ activation and catalyst graphitization were illustrated in Fig. 1. Cheap and commercially available glucose was chosen as the carbon source to synthesize amorphous carbon spheres through hydrothermal carbonization. The as-obtained carbon spheres were then mixed with $K_2FeO_4$ providing activation agent KOH and $Fe(OH)_3$ as eqn (2).

$$4K_2FeO_4 + 10H_2O = 8KOH + 4Fe(OH)_3 + 3O_2 \quad (2)$$

In this step, KOH would react with carbon spheres and develop pores on the surface of samples. The graphitization transformation is as follows: the Fe species are transformed to $Fe_3O_4$ when annealed from 400 °C to 600 °C.[27,28] In the case of 700 °C, $Fe_3O_4$ is converted to metallic Fe as a result of the reduction of amorphous carbon by $H_2$ or CO produced during the pyrolysis process and when the temperature is further increased to 800 °C, graphitized carbon is formed under the catalysis of Fe.[29] Apart from the existence of metallic Fe, a portion of Fe transforms into well-crystallized $Fe_3C$. It was reported that the metallic Fe and pyrolytic carbon lead to the formation of $Fe_3C$.[30,31] Therefore, the results verified that the FC-1-8 sample was consisted of $Fe_3C$/Fe and graphitic carbon. As displayed in Fig. 2a, the diffraction peaks locating at 37.6°, 42.9°, 43.7°and 45.9° correspond to $Fe_3C$ with the standard PDF card of JCPDS no. 35-0772. Two diffraction peaks are detected at 44.6°and 65.0°, which belong to the (110) and (200) planes of Fe (JCPDS no. 06-0696). Furthermore, carbon in the whole process was partly oxidized to $CO/CO_2$ and carbonate and as a result, the porous structure was obtained.[32] Obviously, graphitic carbon could be formed when annealed at the temperature of 800 °C.

To investigate the function of $K_2FeO_4$, carbon spheres annealed without the treatment of $K_2FeO_4$ (FC-0-8) were studied for comparison. From the XRD pattern in Fig. 2a, two relatively broad peaks were existed in the pattern of FC-0-8, implying that the dominant component of the above was amorphous carbon. Validated by the XRD pattern of FC-1-8-HCl, $Fe_3C$/Fe composites were removed successfully. According to the nitrogen adsorption–desorption isotherms plotted in Fig. 2b, FC-1-8-HCl showed IV-type adsorption–desorption isotherm with H4-type hysteresis loop, indicating the presence of mesopores. The SSA of the obtained FC-0-8 is 479.8 $m^2$ $g^{-1}$, while the chemical activation treatment with $K_2FeO_4$ developed more pores making it increased to 545.5 $m^2$ $g^{-1}$ for FC-1-8. FC-1-8-HCl showed the largest SSA up to 2813.6 $m^2$ $g^{-1}$, resulting from the pores caused by the removal of $Fe_3C$/Fe NPs. The pore size distribution in Fig. 2c revealed that the pore diameter of these samples was ~3 nm, suggesting these samples were rich in mesopores.

Raman spectra were conducted to characterize the graphitization degree. Typically, the band at 1350 $cm^{-1}$, known as D-band, is assigned to defect sites or the disordered sp2 carbon. The G band at 1580 $cm^{-1}$ is corresponded to the in-plane vibrational mode of sp2 hybridized carbon.[33] The intensity ratio of $I_D/I_G$ values for FC-0-8, FC-1-8 and FC-1-8-HCl are 1.30, 0.99 and 1.00, respectively (Fig. 2d). Compared with FC-0-8, the lower $I_D/I_G$ values of FC-1-8 and FC-1-8-HCl indicated a relatively short-range order graphitic carbon because of the treatment of $K_2FeO_4$. Furthermore, the X-ray photoelectron spectrum verified the existence of C, O and Fe elements in the surface of FC-1-8 (as illustrated in Fig. 2e).[32] The high-resolution spectra Fe 2p orbit showed two dominant peaks at 711.0 and 713.1 eV, which were indexed to the $2p_{3/2}$ orbitals of $Fe^{2+}$ and $Fe^{3+}$, respectively (Fig. 2f). The peaks located at a binding energy of 724.6 eV, 726.4 eV and 718.5 eV were assigned to $Fe^{2+}$ and $Fe^{3+}$ for the $2p_{1/2}$ band, and a satellite.[34]

To evaluate the surface morphology and structure of the samples, SEM measurements of FC-0-8, FC-1-8 and FC-1-8-HCl were conducted (Fig. 3). After annealed in Ar atmosphere at 800 °C, the as-prepared carbon spheres (FC-0-8) became black and maintained a similar structure and the carbon spheres interconnected forming the 3D network, which was favorable to electron transfer. Besides, FC-1-8 and FC-1-8-HCl generally inherited their structure except for the rough surface of carbon spheres. Furthermore, a comparison of SEM images revealed that the average diameter of the FC-1-8-HCl sample was a little bit smaller than that of FC-1-8 after the removal of $Fe_3C$/Fe NPs. Convinced by the particle size distributions (Fig. S2†), as measured by a statistical method measuring the diameter of 100 particles, the average size of FC-1-8 decreased from ~450 nm to ~240 nm after being etched by HCl.

The TEM images of FC-0-8 presented disordered carbon lattice fringes (Fig. 4a–c), suggesting the existence of amorphous carbon. As shown in Fig. 4d–f, the HRTEM of FC-1-8 was composed of graphitic carbon and Fe NPs. The lattice fringe with a spacing of 0.34 nm corresponded to the (002) plane of carbon and the lattice fringe calculated to be 0.20 nm and 0.24 nm were assigned to the (101) plane of Fe and (111) plane of $Fe_3C$, respectively. Obviously, the existence of metallic Fe contributed to the formation of graphitic carbon. The corresponding elemental mappings of C and Fe further verified that the rough surface of carbon spheres should be $Fe_3C$/Fe NPs (Fig. 4g–i). Part of FC-1-8-HCl NPs showed irregular structure while the HRTEM images in Fig. 4l confirmed the existence of graphitic carbon.

The whole process was economic and environmentally friendly without any toxic or hazardous materials input. FC-1-8 and FC-1-8-HCl were expected to be excellent electrode materials. On the one hand, the partial graphitization with hierarchical porosity structure could offer large SSA value and electroactive sites. On the other hand, the graphitic carbon ensured conductivity of the sample.

### 3.3 Electrochemical performance

Electrochemical properties of the obtained carbon material were examined under a voltage window from −1.2 to −0.3 V at a scan rate of 100 mV $s^{-1}$ initially in a three-electrode configuration. As shown in Fig. 5a, the FC-1-8 electrode displayed a larger area than the other two samples, implying a larger capacitance value. A pair of explicit and symmetrical cathodic and anodic peaks can be observed in the CV curve of FC-1-8, implying a kind of pseudocapacitive behavior. It was reported that $Fe_3C$ species can be oxidized to $Fe_3O_4$ irreversibly in the KOH electrolyte and result in the reversible redox reaction of the newly formed $Fe_3O_4$ material as expressed by the following eqn (3).[21]

$$Fe_3O_4 + 4H_2O + 2e^- \leftrightharpoons 3Fe(OH)_2 + 2OH^- \quad (3)$$

Notably, the graphitic FC-1-8-HCl displayed a much larger integral area than FC-0-8, which convincingly demonstrated excellent energy storage performance. In other words, carbon materials with higher graphitization degree exhibit superior Faraday capacitance. In detail, according to the GCD profiles, the FC-1-8 and FC-1-8-HCl electrodes can deliver the specific capacitance as high as 428.0 and 243.3 F $g^{-1}$ at 1 A $g^{-1}$, whereas the specific capacitance of FC-0-8 are only 84.3 F $g^{-1}$ at 1 A $g^{-1}$ (Fig. 5b). The capacitance value of FC-1-8 outperforms most reported Fe-based carbon materials in Table 2.

The electrochemical impedance spectroscopy (EIS) analysis was carried out to inspect the kinetic properties of these four samples in the range of 0.01 Hz to 100 kHz, the results were delivered in Fig. 5c. It was found that low frequency part of the region was almost straight, implying the low diffusion resistance.[35] In the high frequency part of the EIS plot, FC-1-8 and FC-1-8-HCl display lower $R_s$ values than FC-0-8. It is reasonable that the improved electrochemical performance is related to the higher graphitic degree. The $R_{ct}$ values of 0.21 and 0.22 Ω for FC-1-8 and FC-1-8-HCl were much lower than that of FC-0-8, 0.41 Ω, implying the faster charge transfer at the electrode and electrolyte interface.

As consistent with the CV analysis, the graphitic electrodes of FC-1-8 and FC-1-8-HCl showed a much longer discharge time than the other counterpart demonstrating higher specific capacitance (Fig. S3†). The higher values in specific capacitance can be contributed to the improved conductivity of graphitic carbon, the larger SSA and the porous structure. The CV curves of FC-1-8 at multiple scan rates were accessed in Fig. 5d. CV curves displayed similar shape with the scan rate decreasing from 100 to 5 mV $s^{-1}$ (Fig. 5d). The reduction and oxidation peaks moved outwards as the increase of scan rates due to the polarization of the electrode. The details of galvanostatic charge/discharge curves were exhibited in Fig. 5e. Likewise, the galvanostatic charge–discharge (GCD) curves showing voltage platforms are believed to the nature of pseudocapacitance. FC-0-8 and FC-1-8-HCl exhibited typical rectangular shape of CV curves and triangular GCD curves, demonstrating a double layer electric capacitive behavior (Fig. S4†). The cycle stability was carried out by performing 10 000 times at 5 A $g^{-1}$ (Fig. 5f). FC-1-8 retained a moderate rate of 51.7% compared with the initial capacitance and the inferior cycle stability of FC-1-8 was probably due to the irreversibly oxidized of $Fe_3C$/Fe to $Fe_3O_4$ in KOH electrolyte.[21] The morphology of FC-1-8 and FC-1-8-HCl samples after electrochemical activation were conducted to uncover the mechanism of electrochemical performance (Fig. S5†). It was found that both samples presented spherical structure as before, while FC-1-8 sample showed a relatively smooth surface compared with the initial one. The absence of $Fe_3C$/Fe species resulted in the inferior cycling performance.

## 4. Conclusions

In conclusion, we achieved the transformation from amorphous carbon spheres to graphitic carbon through hydrothermal carbonization, chemical activation and graphitization using $K_2FeO_4$. The obtained FC-1-8 with graphitic carbon and $Fe_3C$/Fe structure are believed to be the promising electrode material. On the one hand, the embedded $Fe_3C$/Fe NPs are contributed to the pseudocapacitance performance with a high specific capacitance of 428.0 F $g^{-1}$ at a discharge current density of 1 A $g^{-1}$. On the other hand, the graphitic carbon could improve the conductivity. When removing $Fe_3C$/Fe NPs, the graphitic carbon of FC-1-8-

HCl with high specific surface area up to 2813.6 $m^2 g^{-1}$ exhibited a high specific capacitance of 243.3 F $g^{-1}$ at 1 A $g^{-1}$.

## Author contributions

Aoping Guo: methodology, validation, formal analysis, investigation, data curation, visualization, writing – original fraft, writing – review & editing. Xiaobao Zhang: methodology, conceptualization, writing – review & editing, data curation. Baiyi Shao: management and coordination, writing – review & editing. Song Sang: methodology, validation, formal analysis, data curation, visualization. Xiaojing Yang: conceptualization, funding acquisition, supervision, visualization, writing – original draft, writing – review & editing.

## Conflicts of interest

The authors declare that they have no known competing financial interests or personal relationships that could have appeared to influence the work reported in this paper.

## Acknowledgements

This work was supported by the National Science Foundation of China (No. 51572031).

## Notes and references

1 C. Zhang, W. Lv, Y. Tao and Q.-H. Yang, *Energy Environ. Sci.*, 2015, **8**, 1390–1403.
2 S. Zheng, J. Ma, Z.-S. Wu, F. Zhou, Y.-B. He, F. Kang, H.-M. Cheng and X. Bao, *Energy Environ. Sci.*, 2018, **11**, 2001–2009.
3 Z. Zhang, M. Qin, B. Jia, H. Zhang, H. Wu and X. Qu, *Chem. Commun.*, 2017, **53**, 2922–2925.
4 Y. Wang and L. Jiang, *ACS Sustainable Chem. Eng.*, 2017, **5**, 5588–5597.
5 F. Veltri, F. Alessandro, A. Scarcello, A. Beneduci, M. A. Polanco, D. C. Perez, C. V. Gomez, A. Tavolaro, G. Giordano and L. S. Caputi, *Nanomaterials*, 2020, **10**, 655.
6 L. L. Zhang and X. S. Zhao, *Chem. Soc. Rev.*, 2009, **38**, 2520–2531.
7 D. Lozano-Castello, D. Cazorla-Amoros, A. Linares-Solano, S. Shiraishi, H. Kurihara and A. Oya, *Carbon*, 2003, **41**, 1765–1775.
8 T. E. Rufford, D. Hulicova-Jurcakova, K. Khosla, Z. Zhu and G. Q. Lu, *J. Power Sources*, 2010, **195**, 912–918.
9 F. Sun, D. Wu, J. Gao, T. Pei, Y. Chen, K. Wang, H. Yang and G. Zhao, *J. Power Sources*, 2020, **477**, 228759.
10 B. Chang, Y. Guo, Y. Li, H. Yin, S. Zhang, B. Yang and X. Dong, *J. Mater. Chem. A*, 2015, **3**, 9565–9577.
11 X. Deng, W. Shi, Y. Zhong, W. Zhou, M. Liu and Z. Shao, *ACS Appl. Mater. Interfaces*, 2018, **10**, 21573–21581.
12 M. Yu, Y. Han, J. Li and L. Wang, *Chem. Eng. J.*, 2017, **317**, 493–502.
13 O. Mykhailiv, H. Zubyk and M. E. Plonska-Brzezinska, *Inorg. Chim. Acta*, 2017, **468**, 49–66.
14 T. Nishida and H. Sueyoshi, *Mater. Trans.*, 2006, **47**, 399–404.
15 Y. Fan, X. Yang, B. Zhu, P.-F. Liu and H.-T. Lu, *J. Power Sources*, 2014, **268**, 584–590.
16 K. Wang, Y. Cao, X. Wang, P. R. Kharel, W. Gibbons, B. Luo, Z. Gu, Q. Fan and L. Metzger, *Energy*, 2016, **101**, 9–15.
17 B. Li, P. Gu, Y. Feng, G. Zhang, K. Huang, H. Xue and H. Pang, *Adv. Funct. Mater.*, 2017, **27**, 1605784.
18 K.-B. Wang, Q. Xun and Q. Zhang, *Energychem*, 2020, **2**, 100025.
19 S. Zheng, Y. Sun, H. Xue, P. Braunstein, W. Huang and H. Pang, *Natl. Sci. Rev.*, 2021, DOI: 10.1093/nsr/nwab197.
20 S. Zheng, Q. Li, H. Xue, H. Pang and Q. Xu, *Natl. Sci. Rev.*, 2020, **7**, 305–314.
21 L. Hou, W. Yang, X. Xu, B. Deng, Z. Chen, S. Wang, J. Tian, F. Yang and Y. Li, *Chem. Eng. J.*, 2019, **375**, 122061.
22 B. Ni, R. Chen, L. Wu, P. Sun and T. Chen, *Sci. China Mater.*, 2021, **64**, 1159–1172.
23 L. Chai, Z. Hu, X. Wang, L. Zhang, T.-T. Li, Y. Hu, J. Pan, J. Qian and S. Huang, *Carbon*, 2021, **174**, 531–539.
24 Z. Nie, Y. Wang, Y. Zhang and A. Pan, *Sci. China Mater.*, 2016, **59**, 247–253.
25 Z. Gao, Y. Zhang, N. Song and X. Li, *Mater. Res. Lett.*, 2017, **5**, 69–88.
26 X. M. Sun and Y. D. Li, *Angew. Chem., Int. Ed.*, 2004, **43**, 597–601.
27 C. Song, H. Kuihua, Y. Gao, Z. Teng, M. Wang and J. Li, *J. Electrochem. Soc.*, 2020, **167**, 160549.
28 P. Yunjie, S. Yang, J. Han, X. Li, H. Zhang, B. Xiong, P. Fang and C. He, *Electrochim. Acta*, 2021, **380**, 138237.
29 Y. Gong, D. Li, C. Luo, Q. Fu and C. Pan, *Green Chem.*, 2017, **19**, 4132–4140.
30 J. Li, N. Wang, J. Deng, W. Qian and W. Chu, *J. Mater. Chem. A*, 2018, **6**, 13012–13020.
31 S. Esconjauregui, C. M. Whelan and K. Maex, *Carbon*, 2009, **47**, 659–669.
32 X. Dong, J. Wang, M. Yan, B. Ren, J. Miao, L. Zhang, Z. Liu and Y. Xu, *Ceram. Int.*, 2021, **47**, 5998–6009.
33 Y. Hou, T. Huang, Z. Wen, S. Mao, S. Cui and J. Chen, *Adv. Energy Mater.*, 2014, **4**, 400337.
34 J. Li, X. Li, H. Chen, D. Xiao, J. Li and D. Xu, *J. Electroanal. Chem.*, 2020, **865**, 127421.
35 F. Zhang, T. Liu, G. Hou, T. Kou, L. Yue, R. Guan and Y. Li, *Nano Res.*, 2016, **9**, 2875–2888.
36 A. Kumar, D. Das, D. Sarkar, S. Patil and A. Shukla, *J. Electrochem. Soc.*, 2020, **167**(6), 060529.
37 G. Li, J. Zhang, W. Li, K. Fan and C. Xu, *Nanoscale*, 2018, **10**, 9252–9260.
38 L. Yao, J. Yang, P. Zhang and L. Deng, *Bioresour. Technol.*, 2018, **256**, 208–215.
39 J. Liu, X. Kang, X. He, P. Wei, Y. Wen and X. Li, *Nanoscale*, 2019, **11**, 9155–9162.
40 Y. Wang, G. Zhang, G. Liu, W. Liu, H. Chen and J. Yang, *RSC Adv.*, 2016, **6**, 44013–44018.